FUNDAMENTALS & APPLICATIONS

CHEMELECTROCHEM

ANALYSIS & CATALYSIS, BIO & NANO, ENERGY & MORE

Accepted Article

Title: High-Voltage Performance of Ni-Rich NCA Cathodes: Linking Operating Voltage with Cathode Degradation

Authors: Lamuel David, Debasish Mohanty, Linxiao Geng, Rose E. Ruther, Athena S. Sefat, Ercan Cakmak, Gabriel M. Veith, Harry M. Meyer III, Hsin Wang, and David L. Wood, III

This manuscript has been accepted after peer review and appears as an Accepted Article online prior to editing, proofing, and formal publication of the final Version of Record (VoR). This work is currently citable by using the Digital Object Identifier (DOI) given below. The VoR will be published online in Early View as soon as possible and may be different to this Accepted Article as a result of editing. Readers should obtain the VoR from the journal website shown below when it is published to ensure accuracy of information. The authors are responsible for the content of this Accepted Article.

To be cited as: *ChemElectroChem* 10.1002/celc.201901338

Link to VoR: http://dx.doi.org/10.1002/celc.201901338

A Journal of ChemPubSoc Europe

WILEY-VCH

www.chemelectrochem.org

10.1002/celc.201901338

High-Voltage Performance of Ni-Rich NCA Cathodes: Linking Operating Voltage with Cathode Degradation

Dr. Lamuel David,[a] Dr. Debasish Mohanty,[a] Dr. Linxiao Geng,[a] Dr. Rose E. Ruther,[a] Dr. Athena S. Sefat,[b] Dr. Ercan Cakmak,[b] Dr. Gabriel M. Veith,[b] Dr. Harry M. Meyer III,[b] Dr. Hsin Wang,[b] Dr. David L. Wood III[a,c] *

[a]Energy and Transportation Science Division, Oak Ridge National Laboratory, Oak Ridge, Tennessee, 37831, USA

[b]Materials Science and Technology Division, Oak Ridge National Laboratory, Oak Ridge, Tennessee 37831, USA.

[c]Bredesen Centre for Interdisciplinary Research and Graduate Education, University of Tennessee, Knoxville, Tennessee 37996, USA

Correspondence and requests for materials should be addressed to D.L.W. (wooddl@ornl.gov)

Manuscript for submission to *ChemElectroChem*

This manuscript has been authored by UT-Battelle, LLC under Contract No. DE-AC05-00OR22725 with the U.S. Department of Energy. The United States Government retains and the publisher, by accepting the article for publication, acknowledges that the United States Government retains a non-exclusive, paid-up, irrevocable, world-wide license to publish or reproduce the published form of this manuscript, or allow others to do so, for United States Government purposes. The Department of Energy will provide public access to these results of federally sponsored research in accordance with the DOE Public Access Plan (http://energy.gov/downloads/doe-public-access-plan).

Keywords: Li-ion battery, Ni-rich cathodes, electrochemistry, magnetic susceptibility, *in-situ* XRD

Accepted Manuscript

This article is protected by copyright. All rights reserved.

10.1002/celc.201901338

Abstract

High voltage Ni-rich cathodes have been studied as a possible way to achieve high energy density in Li-ion batteries. However, capacity fade due to structural changes at high voltages has limited their applications. This study identifies 4.5V (vs. graphite) as the optimum upper cutoff voltage (UCV) for a Ni-rich NCA cathode [$LiNi_{0.8}Co_{0.15}Al_{0.05}O_2$]. At this UCV, NCA delivers a 12% increase in reversible capacity (when discharged to 2.5 V) and retains 92% of its initial capacity after 100 cycles at 1C/-1C cycling when compared to 4.2 V as UCV. By increasing UCV to 4.7V, the discharge capacity can be raised to >200mAh/g. However, the rate of capacity fade is greater when compared to 4.5V as UCV. This increased rate of capacity fade, at higher UCV, is related to irreversible lattice contractions that leads to structural rearrangement at charged states during high-voltage cycling. Our results show a change in transition metal oxidation states and an onset of structural ordering occurs when the UCV is 4.7 V.

Accepted Manuscript

This article is protected by copyright. All rights reserved.

1. Introduction

Lithium-ion batteries (LIBs) are widely considered as the major source of energy storage for powering consumer electronics and electric vehicles because of high-energy density.[1-7] In contrast to consumer electronic devices in which batteries are replaced every few years, batteries in electric vehicle (EVs) and plug-in hybrid electric vehicles (PHEVs) are expected to be in use for over a decade.[8] These requirements along with increasing demand for higher range in EVs requires significant improvements in volumetric and gravimetric energy density, cycle life and safety characteristics of LIBs. As a result, extensive research in meeting these challenges has been focused on developing high-energy cathodes that provide increased capacity (>200 mAh/g).[5,9] In this regard, Ni-rich cathodes such as $LiNi_{0.8}Co_{0.15}Al_{0.05}O_2$, conventionally referred to as NCA, has been commercialized.[10-15] NCA adopts a layered *R-3m* lattice structure like $LiNiO_2$ in which Co^{3+} and Al^{3+} are substituted for Ni^{3+} in octahedral sites to stabilize the layered structure and to improve the thermal stability and capacity retention, respectively.[10,11] These layered cathodes have shown high reversible initial capacities within the 3.0-4.2 V window,[12] and a 25% increase in capacity was observed when cycled to above~4.8 V.[5]

During battery cycling, at certain upper cutoff voltages (UCVs), like 4.1V,[16] the structure of NCA transforms from a layered *R-3m* structure to a spinel *Fd-3m* phase and/or insulating NiO phase (which is a rock-salt *Fm3m*structure) on the particle surface, resulting in increased interfacial resistance and poor cycle life.[17] These phase transformations may also be accompanied by a release of oxygen,[18] which when combined with electrolyte in the battery can lead to thermal run away and/or thicker cathode electrolyte interface (CEI) layer.[11] Extensive research into the exact mechanism of these reactions in Ni-rich cathodes has been conducted using time-resolved X-ray diffraction (XRD),[11,17,19-22] X-ray absorption spectroscopy (XAS),[23] nuclear magnetic resonance (NMR)[24] and several other analytical techniques.[25] Previous studies on NCA materials are based on *ex-situ* analysis of the electrode; moreover, the *in-situ* (XRD)analysis that has been reported is mostly on transformations that occur during thermal annealing of charged/discharged cathodes, and to our understanding, few reports are on observation of dynamic structural changes during the charge-discharge process in other Ni-rich systems.[20] Nonetheless, early detection of this structural changes in NCA at higher UCV is crucial to predicting degradation over the repeated cycling and stability of this cathode material in a battery.

Therefore, in this report our goal is to: i) first compare the electrochemical performance of NCA at different UCVs; 4.2V, 4.4V, 4.5V, and 4.7V (in a full-coin cell) to find the optimum high-voltage UCV

Accepted Manuscript

This article is protected by copyright. All rights reserved.

for stable electrochemical performance; and ii) understand the mechanism(s) for capacity fading beyond that optimum UCV. To understand capacity degradation mechanism(s), we employed combined ex-situ/in-situ XRD and ex-situ temperature dependent magnetic susceptibility technique to evaluate structural modifications in NCA when charged to higher UCV (4.7V) during the first cycle and correlate these findings to voltage and capacity decay during cycling. While in-situ XRD provides the dynamic crystalline structural changes in NCA, ex-situ magnetic susceptibility provides the onset of any additional phase formation (even before the phase attains crystallinity).

2. Experimental Section

2.1 Materials

The $LiNi_{0.80}Co_{0.15}Al_{0.05}O_2$ (NCA) pristine powder material in this study was purchased from TODA America and was used as the cathode. A12 graphite powder was purchased from Conoco Phillips and used as the anode. Subsequently, single sided electrodes were fabricated at the DOE Battery Manufacturing Facility (BMF) at Oak Ridge National Laboratory. The cathode composition was 90 wt% NCA, 5wt% Solvay 5130 PVDF binder (8% in NMP) and 5 wt% Super P1 Carbon Black (Timcal). The mass loading of NCA electrode was approximately 12.0 mg/cm^2. Drying and calendering at 0.5 m/min resulted in 37% porosity cathodes with 65 mm thick coatings. The anode composition was 92 wt% A12 graphite, 4 wt% Solvay 5130 PVDF binder (8% in NMP) and 4 wt% Super P1 Carbon Black (Timcal). Drying and calendering at 0.5 m/min resulted in 37% porosity cathodes with 65 mm thick coatings. The electrolyte was a 1.2 M solution of $LiPF_6$ in ethylene carbonate (EC) and ethyl methyl carbonate (EMC) (3:7 ratio by weight) (SoulBrain, MI).

2.2 SEM and X-ray diffraction (XRD) on pristine powder

The scanning electron microscopy (SEM) images and energy dispersive spectroscopy (EDS) were obtained by a Hitachi S4800 FEG-SEM at 20 kV. The *ex-situ* powder XRD patterns were collected on the PANalytical X'Pert Pro system, the same instrument which was used for the *in-situ* XRD study. The experimental data collection was similar to the conditions for *in-situ* XRD experiments. Post-test characterization was performed on electrodes that were harvested from cells that underwent long term cycling. The cells were disassembled in an Ar filled glove box and rinsed with EMC for 2 minutes to remove residual electrolyte and Li salt.

This article is protected by copyright. All rights reserved.

Accepted Manuscript

2.3 In-situ XRD

An *in-situ* XRD cell was fabricated with2032 coin cell hardware based on a modified procedure described earlier by our group.[26,27] This cell was constructed by punching a hole (~13 mm diameter) in the regular coin cell case and then sealed with Kapton® film (Ø19 mm disk), and vacuum sealing epoxy (Torr Seal®) was applied along the edge of the window to prevent electrolyte leakage. Comparison of charge-discharge curves from windowed and non-windowed cells showed no significant difference, so the Kapton windows were considered gastight and the *in-situ* XRD results as representative of the cell behavior. The modified coin cell case was transferred to an argon filled glove box for coin cell assembly with NCA (Ø12 mm disk) as the cathode and lithium foil (Ø12 mm disk, Alfa Aesar, 0.75 mm thick, 99.9%) as the anode, respectively. A solution of 1.2 M lithium hexaflurophosphate ($LiPF_6$) in ethylene carbonate (EC):ethyl methyl carbonate (EMC) (3:7 wt fraction) was used as the electrolyte (SoulBrain). A Celgard 2325 separator (16 mm diameter) was used between the electrodes. Electrochemical cycling was performed using a BioLogic SP-200 potentiostat controlled with the EC-Lab software (V. 10.02). X-ray patterns were collected simultaneously using a PANalytical X'Pert Pro system with molybdenum source (l = 0.71073 Å), and automatic divergence and anti-scatter slits operated at 60 kV and 45 mA. The charge/ discharge process was carried out between 2to 4.8 V vs. Li/ Li^+ at C/20 rates. XRD patterns were collected with 2θ angle range of 5–37.5°at a rate of one scan per hour. The collected *in-situ* XRD patterns were refined by the Rietveld method using X-pert HighScore Plus with zero sample displacement errors and available background correction. The lattice constants were determined by least squares refinements.

2.4 Ex-situ magnetic susceptibility

DC magnetization was measured as a function of temperature, using a Quantum Design Magnetic Property Measurement System. Each sample was first cooled to 5 K in zero field, then a field of 100 *Oe* was applied, and the data were collected from 5 K to 320 K (ZFC). The sample was also cooled in the applied field from 320 K down to 5 K, while measuring magnetic moments (FC). Magnetization data were collected from the electrodes after cycling. The cycled electrodes were washed in DMC to remove any remaining electrolyte and decomposition products. There was no significant difference in the weight of the washed cycled electrodes compared to as-coated electrodes. The effective magnetic moments were calculated from the molar mass of the active material. Magnetic susceptibility was collected from NCA during the first cycle vs. Li/Li^+ at 4.7V (charged state) and 2.5 V (discharged state). Subsequently,

This article is protected by copyright. All rights reserved.

Accepted Manuscript

magnetic susceptibility was collected at discharged state (2.5V) after 120 charge-discharge cycles at two different UCVs (4.5V and 4.7V).

2.5 Electrochemical testing

The electrochemical cycling was performed by using a BioLogic SP-200 potentiostat controlled with the EC-Lab software (V. 10.02). Coin cells were assembled with NCA (Ø12 mm disk) as the cathode and A12 graphite (Ø12 mm disk) as the anode. A solution of 1.2 M lithium hexaflurophosphate ($LiPF_6$) in ethylene carbonate (EC):ethyl methyl carbonate (EMC) (3:7 wt fraction) was used as electrolyte (SoulBrain). A Celgard 2325 separator (16 mm diameter) was used between the electrodes. The cells were cycled between 2.5V as the lower cutoff voltage (LCV) and 4.2 V, 4.4 V, 4.5 V, 4.6 V and 4.7V as the upper cutoff voltages (UCVs). Three cells were prepared for each voltage window, resulting in 15 cells each for both the rate capability test and the cycle life test, respectively. All cells underwent a formation protocol for the first two cycles with a current rate of C/20 during both charging and discharging steps. The rate capability test protocol was as follows: charge current was constant with a C-rate of C/10, while the discharge current rate was increased from C/10, C/5, C/2, 1C, 2C and 5C for 5 cycles each, and returned to C/10 C-rate for the last 5 cycles. For the cycle life test the cells were cycled at their respective voltage windows with a current rate of 1C during both charging and discharging steps. All cycles followed constant current/constant voltage (CC/CV) up to a residual current rate of C/20during the charging step and constant current (CC) during the discharging step. Each data point represents the average of 3 cells with a 2σ standard deviation error bar.

2.6 X-ray Photoelectron Spectroscopy (XPS)

XPS was performed using a Thermo Scientific (Waltham, MA, USA) Model K-Alpha XPS instrument. The instrument utilizes a monochromated, micro-focusing, Al Kα X-ray source (1486.6 eV). Analyses of the samples were all conducted with a 400 µm X-ray spot size for maximum signal and to obtain an average surface composition over the largest possible area. The instrument has a hemispherical electron energy analyzer equipped with a 128 multi-channel detector system. The base pressure in the analysis chamber is typically 2 x 10^{-9} mbar or lower. The samples were transferred from an argon filled glove box in a special vacuum transfer system to the XPS instrument to prevent air exposure. Specific areas were chosen for analysis by viewing the samples with a digital optical camera with a magnification of approximately 60-200X.

This article is protected by copyright. All rights reserved.

Accepted Manuscript

2.7 Differential Scanning Calorimetry (DSC)

Differential scanning calorimetry (DSC) analysis was performed on a Netzsch 449instrument. To prepare the samples for DSC experiment, the cells under different UCV conditions were charged one last time to 4.5 V. The coincells then were disassembled in an argon glovebox. The electrodes were thoroughly rinsed with DMC three times to remove the electrolyte. Then the NCA powders were scraped off the current collector. The powders were then sealed in a stainless-steel high-pressure capsule (Perkin Elmer) with fresh electrolyte (electrolyte:powder 1µl/mg). Samples were heated from 20 to 350°C at 10°C/min in argon.

3. Results

3.1 Structure of pristine NCA powder; layered O3 phase

Before attempting to study the cycling behavior, pristine NCA material was evaluated by X-ray diffraction (XRD) and scanning electron microscopy (SEM). The SEM images (Figure 1a-b) showed that the secondary particles were spherical in shape with an average particle size of 5±2μm (Figure 1c). The high magnification SEM image in Figure 1b shows the primary particles are between 200-400 nm. The EDS analysis (Figure 1d) of the particle confirmed the composition of the material to be $LiNi_{0.8}Co_{0.15}Al_{0.05}O_2$. The XRD data in Figure 1eshows the pristine NCA material is layered (O3) phase with R-3m (rhombohedral) space group as reported in previous literature.[11,19]

3.2 Structure of NCA at the end of first cycle charge and discharge (4.7 V charged and 2.5V discharged); onset of pronounced transition metal ordering

In the next step of this investigation, we employed *ex-situ* magnetic susceptibility to investigate the structural changes during the first cycle. As magnetic susceptibility measurements are sensitive to transition metal ordering and oxidation states (detection limit of 10^{-6} EMU for short-range magnetic amorphous and nanocrystalline phase), any change in structural rearrangement due to relocation of transition metal ions or change in oxidation states can be detected by magnetic susceptibility experiments. This method is well established in the literature.[28]

Comparison of molar magnetization (χ) ($\chi = M/H$, M is the magnetic moment and H = 100 Oe is the applied external magnetic field) at zero field cooling-ZFC (solid pattern) and field cooling-FC (hollow pattern) modes of (1) pristine NCA electrode, (2) NCA electrode harvested from cell that was charged to 4.7 V during first cycle and (3) NCA electrode harvested from cell that was charged to 4.7V and

This article is protected by copyright. All rights reserved.

Accepted Manuscript

discharged to 2.5 V at the end of first cycle are shown in Figure 2(a). As explained in the literature, if FC and ZFC follows the same path, the magnetic interaction among transition metal ions is paramagnetic (for example: $LiCoO_2$).[29] Divergence between FC and ZFC at lower temperature provides the signature for magnetic ordering and the nature and strength of divergence indicate the anti-ferromagnetic/ferromagnetic signature for the frustrated lattice (for example: Li_2MnO_3 or $LiNiO_2$).[30,31]

From the magnetic susceptibility experiments, notable observations were made:

Pristine NCA electrode:

- FC and ZFC curves followed the same path and divergence of the curves occurred at ~8 K.
- An increase in magnetic susceptibility was observed when $T \leq 50$ K.
- The effective magnetic moment (μ_{eff}) was2.736 BM.

NCA electrode charged to 4.7V:

- FC and ZFC curves followed the same path.
- An increase in magnetic susceptibility was observed when $T \leq 50$ K; however, the magnitude of magnetic susceptibility was lower compared to pristine NCA.
- The effective magnetic moment was1.786 BM.

NCA electrode charged to 4.7V and discharged to 2.5V at the end of first cycle:

- FC and ZFC curves followed the same path; however, a strong indication of bifurcation or divergence of these curves was observed at~13 K.
- An increase in magnetic susceptibility was observed when $T \leq 50$ K; the magnitude of magnetic susceptibility was lower than the pristine NCA and higher than NCA harvested at the 4.7 V charged state.
- The effective magnetic moment was2.037BM.

At high temperature ($T \geq 100$ K), all samples showed paramagnetic behavior; indicating that the magnetic moments of transition metal ions are randomly oriented and similar to the phenomenon observed for$LiCoO_2$, $LiNi_{1/3}Mn_{1/3}Co_{1/3}O_2$, and Li-rich cathodes. An increase in the magnitude of magnetic susceptibility values are an indication of ferro/ferri-magnetic interaction among transition metal ions; which was also observed in the case of other layered oxide systems. However, the divergence/bifurcation of FC and FZC is atypical phenomenon, and it indicates anti-ferromagnetic

This article is protected by copyright. All rights reserved.

Accepted Manuscript

magnetic ordering or a presence of "frustrated lattice" in the host oxides. The appearance of FC and ZFC bifurcation at 8 K in the pristine material may suggest a presence of frustrated antiferromagnetic ordering as also observed for $LiNiO_2$.[31] This type of magnetic ordering is an indication of the presence of Ni in Li-layer in a trigonal (O3) lattice. The divergence of FC and ZFC in the case of NCA electrode discharged to 2.5Vis more pronounced and occurs at higher temperature (~13 K) than pristine NCA. This indicates the onset of a (strong) antiferromagnetic ordering and irreversible structural change that could impact long-term cycling performance (refer to electrochemical data in next section) when cycled at an UCV of 4.7V. These structural changes in bulk NCA may not bean "additional" spinel/NiO-type phases, but they provide an evidence of relocation and/or change in oxidation states of transition metal ions in the lattice indicating the presence of a structural ordering. The onset of this structural ordering will have an impact on the lithium transport process, as it alters the original host NCA structure.

The effective magnetic moment of pristine NCA deduced from the Curie constant C_p obtained from the inverse susceptibility *vs* temperature in the range of 150 K to 300 K is 2.736 BM. The effective magnetic moment decreases to 1.786 BM at the 4.7 V charged state; indicating the oxidation of Ni^{3+} to Ni^{4+}. After discharging to 2.5 V, the magnetic moment value is 2.037 BM, a value which is less than the pristine NCA. This result indicates that average oxidation state of transition metal ions is not the same as pristine NCA, which means that some of the oxidized Ni^{4+} ions may not reduce back to Ni^{2+}.

The negative values of the Curie-Weiss temperature (Figure 2b) for pristine NCA shows some degree of antiferromagnetic (AF) nature, which may not be an indication of a secondary (spinel) phase in pristine NCA; however, it was interesting to note that the AF nature increases at 4.7Vcharged state and decreases at 2.5 V discharged state. The Curie-Weiss temperature at the 2.5 V discharged state was slightly more negative than pristine NCA.

In summary the magnetic susceptibility experiment from the harvested cathode (UCV = 4.7 V and LCV = 2.5 V vs. Li/Li^+) shows:

1. Pronounced structural ordering after fist cycle discharging.
2. The average oxidation state of TM ions does not remain the same as pristine NCA.

3.3 Structural modification during first charge-discharge cycle; c-lattice contraction when charge voltage is ≥4.15V

This article is protected by copyright. All rights reserved.

Accepted Manuscript

To obtain a deeper understanding in NCA structural modification during first cycle, in the next step, we employed *in-situ* XRD during first charge-discharge cycle. The goal was to identify and monitor the structural changes that might occur when NCA is charged to higher upper cut-off voltages (UCVs) beyond 4.1V. The contraction of the lattice along the *c*-axis during charging may indicate some degree of structural modifications of NCA, but, may not have an immediate impact on capacity fade.[32-34] However, if the structure undergoes a severe degree of contraction (for example when UCV ≥4.6V), immediate capacity fading is observed (see section 3.4 below).

Figure 3shows*in-situ* XRD from a half-coincell collected during the first charge-discharge cycle. XRD data was collected during charging up to 4.8V and discharging to 2.0 V. For simplicity, the XRD scans are divided into four sections for ease of analysis based on major changes in peak positions as shown in Figure 3: "Ch1" is the 1st cycle charge section between open circuit voltage 3.46-4.15 V, "Ch2" is 1st cycle charge section between 4.15-4.8 V, "Disch1" is 1st cycle discharge section between 4.8-4.05 V and "Disch2" is 1st cycle discharge section between 4.05-2.0 V. The corresponding voltage profile with the color code for the four different sections during charge and discharge is also shown in the insert of Figure 3. All the characteristic peaks such as (003), (101), (012), (108) and (110) Bragg reflections associated with the rhombohedral phase were indexed which was similar to the XRD of pristine powder obtained using *ex-situ* XRD.

In order to track the lattice contraction and expansion along the *c*-axis during charging and discharging, the (003) peak was examined. The magnified intensity plot of (003) *c*- and *a*-lattice parameter values during charging and discharging process is shown in Figure 4 and 5, respectively. During the Ch1 range (3.46 to 4.15 V), the 2θ value of (003) peak shifted to lower 2-theta values, corresponding to an increase in *c*-lattice. However, during the Ch2 range the 2θvalues of (003) increased significantly, which indicates a decrease in *c*-lattice parameters. Correspondingly, the *c*-lattice expanded during Disch1 and contracted during Disch2. It was also found that the *a*-lattice parameter decreased during Ch1 and Ch2 regions and increased during Disch1 and Disch2.

An increase in the *c*-lattice indicates the expansion of the NCA crystalline structure along the *c*-axis; which is typical in oxide cathode systems. The process of removing Li-ions from the host structure during charging increases the electrostatic repulsion in cubic-closed-packed oxygen layers and lattice expansion along *c*- axis occurs. When the charging voltage is ≥4.15V the lattice contracts; a phenomenon that is also observed in other cathode oxide systems, but at different charging voltages. For

This article is protected by copyright. All rights reserved.

Accepted Manuscript

example, in the case of $LiCoO_2$, lattice contraction occurs when the UCV ≥ 4.45 V (vs. Li/Li^+); indicating a phase transition from O3-H13.[35] In Li-rich systems, lattice contraction occurs at ~4.45 Vindicating the oxygen participation/release at high voltage.[36] In this work, the NCA lattice contraction at 4.15 V may indicate the gliding of lattice planes due to atomic structural rearrangement/modification. This phenomenon may not completely destroy the lattice structure in the first cycle, as the structure retains the initial *c*-lattice parameter value when the discharge voltage is at 3.0 V (Figure 5).However, extent of lattice contraction (at higher UCV) may initiate permanent altering of the host NCA structure and cause an increase in capacity fading rate. These structural changes can also be the cause for adverse changes in the lattice that was also observed in magnetic susceptibility measurements (see previous section). It should be noted that no additional (for example spinel, NiO) phases were detected during first charge-discharge cycle by in-situ XRD in this study. Moreover, the effect of high UCV on the bulk morphology of NCA electrode were investigated using SEM. No significant differences were observed between pristine electrode and electrodes cycled with UCV of 4.5V and 4.7V. (See SEM images in the supplementary information Figure S1)

In summary:

1. *In-situ* XRD showed when charging beyond a UCV of4.15V (vs. Li/Li^+), NCA lattice contraction occurred.
2. During discharge, the expanded lattice regains its original lattice parameters (which was at OCV) when the LCV was ≤3.0V (vs. Li/Li^+)
3. Irreversible phase transition (in bulk NCA) was not detected by *in-situ* XRD.

3.4 Electrochemical performance of NCA at high voltages; stable performance at 4.5V UCV cycling

To study the effect of UCV on capacity fading, full-cells (N/P ratio was maintained between approximately 1.1 to 1.3) with NCA as the cathode were tested with varying UCVs of 4.2 V, 4.4 V, 4.5 V, 4.6 V, and 4.7V. Capacity fading profiles (up to 120 cycles) are shown in Figure 6. From here onward, the cells cycled to 4.2 V, 4.4 V, 4.5 V, 4.6 V and 4.7V are named as NCA42, NCA44, NCA45, NCA46 and NCA47, respectively. In Table 1 the first cycle discharge capacity of the full cells cycled to different UCVs (cycled at C/20) and their coulombic efficiencies are shown. These results clearly show that with slow charging and discharging rates of C/20, the cell cycled to 4.7 V had the highest first cycle reversible capacity of 259 mAh/g and the capacity decreased to 224 mAh/g, 205 mAh/g, 204 mAh/g and

This article is protected by copyright. All rights reserved.

Accepted Manuscript

184mAh/g for NCA46, NCA45, NCA44 and NCA42, respectively. However, the first cycle efficiency was ~86% for all the cells irrespective of the UCV.

The cycle life testing at 1C/-1Cshowedanincrease in initial discharge capacity with increasing UCV. The discharge capacity profiles clearly show stable cycling performance for NCA42, NCA44, NCA45 and significant capacity fading rate for NCA46, and NCA47. NCA45 shows 12% increase in discharge capacity as compared to NCA42 with stable cycle life (92% capacity retention) after 120 cycles in a full-coin cell. In order to investigate the voltage profiles during cycling, the charge-discharge profiles were normalized and are shown in Figure 7. NCA42 and NCA44 show stable voltage profiles, whereas minimal voltage profile decay is observed in case of NCA45. However, NCA46 and NCA47 show significant voltage decay. As the UCV increased to 4.5V, 4.6V, and 4.7V, the IR drop features became significant. Major IR drop may be a contributor for capacity fading at 4.6 V and 4.7V UCV along with structural rearrangement (see section 3.5 and 3.6);however, quantification of these contributions cannot be made in the scope of this work.

In summary;

1. NCA when cycled to4.5V UCV (vs. graphite), showed a discharge capacity enhancement of 12% as compared to the cycling at 4.2V UCV and 92% capacity retention; minimal voltage profile decay over 120 cycles at 1C/-1C cycling conditions in a full coin cell was observed.
2. Cycling beyond 4.5V (4.7V vs. graphite) increased the discharge capacity; however, severe capacity fading and voltage profile decay was observed.

In order to understand the capacity degradation when UCV >4.5V, post cycling characterization on NCA45, NCA47 was conducted.

3.5Modifications of NCA structure after cycle-life testing; presence of strong antiferromagnetic ordering:

The ex-situ magnetic susceptibility of NCA after long-term cycling at 4.5 V and 4.7 V UCV were compared with pristine electrodes in Figure 8. All the cells were discharged completely to 2.5 V before disassembling. A notable decrease in magnetic moment was observed forNCA47, and the Curie-Weiss fit of the paramagnetic region also confirmed that the effective magnetic moment was1.574BM. The effective magnetic moment in the pristine and NCA45 was2.736BM and 2.09BM, respectively. This decrease in magnetic moment suggests that the average oxidation states of TM ions in the discharged

This article is protected by copyright. All rights reserved.

Accepted Manuscript

NCA45and NCA47 do not remain the same as for the pristine NCA. The higher the deviation from pristine NCA values, the greater the degree of change in the average TM oxidation states, as was observed for NCA47. In addition, the Curie-Weiss temperature (in Figure 8a) shows a significant increase in negative values forNCA47, which is indicative of pronounced antiferromagnetic ordering in the NCA lattice. Antiferromagnetic ordering is not necessarily confirmation of formation ofa spinel phase in the bulk; however it may be an indication of onset of a lattice with a strong antiferromagnetic ordering, which would grow during prolonged cycling for spinel or "spinel-like" phase formation.

In summary,

1. Significant changes in average oxidation state of TM ions and strong anti-ferromagnetic ordering were observed in NCA when cycled to4.7V UCV.

3.6 Structure of bulk NCA after cycle life testing; no spinel or spinel-like phase was observed

Ex-situ XRD partterns from NCA45 and NCA47 after cycle life testingalong with pristine NCApowder are shownin Figure 9.It is evidant that the NCA cathode does not show any distinguished spinel or spinel-like phase (in bulk NCA). It should be noted that the (006) peak intensity wassignificantly reduced in case of NCA47. This finding is an indication of alternation of the layered O3 structure. The (003) peak of NCA45 attainedalmost the same *d*- spacing as pristine NCA powder. In contrast, NCA47 shows the shifting of (003) peak to lower *d*- spacing. These structural changes corelate well to the changes observed in *ex-situ*mangnetic susceptability data for these samples. The increase in *c*-lattice parameter for thecase of NCA47 shows the irreversible loss of lithiumions duringcycling, which is also in agrement with the capacity fading observations for NCA47 after 120 cycles as compared to NCA45.

In summary,

1. NCA cycled to4.7V UCV shows significant lattice expansion along the *c*- axis indicating a lithium-deficient O3 phase.
2. NCA cycled to4.7 V UCV shows a disappearance of the (006) peak indicating alternation of O3 structure.
3. No spinel or spinel-like phase was observed in bulk NCA structure cycled to4.7V.

4. Discussion

Pristine NCA material (studied here) is a layered (O3) structure with Li/Ni interchange in the respective layers (Figure 2a). This Li/Ni interchange is suppressed during cycling as is evident from Figure 8a. Therefore, the presence of Li/Ni interchange in the pristine NCA may not deteriorate the performance if

This article is protected by copyright. All rights reserved.

Accepted Manuscript

cells are operated at optimum UCV (4.5V in this case). Based on this study, 4.5V was identified as optimum UCV for NCA, where a 12% improvement of discharge capacity (when discharged to 2.5 V) was observed as compared to 4.2VUCV, and 92% capacity retention was measured after 120 cycles at 1C/-1C cycling conditions. It was also observed that increasing the UCV to 4.7V the capacity of NCA can reach to 259mAh/g at a discharge rate of C/20, which is a 20% capacity improvement compared to the 4.2V UCV. However, capacity fading increases substantially under these operating conditions. No "distinguished" additional phase was observed from bulk NCA harvested from the 4.7V UCV cell; however, the onset of a lattice with "anti-ferromagnetic" ordering and significant alternation of TM ion oxidation states were observed. A much higher amount of cation and lithium loss was observed on the surface of NCA particles cycled at 4.7V-2.5V as compared to NCA cycled at 4.5-2.5V (See XPS results in supplementary information Figure S2), which indicates substantial loss of lithium and cation relocation/migration to the surface altering the host NCA structure (See Figure S5). Only a slight difference in the onset of exothermic reaction temperature was observed in NCA cycled to an UCV of 4.7V (238°C) as compared to UCV of 4.5V (240°C) indicating similar thermal stability characteristics of NCA cycled at 4.5V and 4.7V as UCV (See supplementary information Figure S3). It is important to note that the electrodes for the *ex-situ* magnetic susceptibility study were harvested from fully discharged cells. Interestingly, the magnetic behavior of the NCA47 electrode in Figure 8(b) closely resembles the properties observed for the fully charged electrode as shown in Figure 2(b). Even though there was no significant structural change in *ex-situ* XRD after cycling, the repeated minor change in NCA structure during continued cycling to 4.7 V UCV led to a permanent change in magnetic susceptibility causing irreversible capacity fade. We do acknowledge electrolyte instability also contributes to capacity fade, and the combination of structural changes and electrolyte oxidation at high UCV could further accelerate the rate of performance decay.

5. Conclusions

Conclusions from this work are:

1. The study showed that the magnetic properties of NCA are sensitive to structural changes that occur during cycling at higher UCVs and are responsible for causing irreversible capacity fade.
2. Cycling at UCV >4.5V results in severe capacity fading; however, no distinguishable additional phases were observed in bulk NCA after 120 cycles.

This article is protected by copyright. All rights reserved.

Accepted Manuscript

3. Lattice stability of NCA at high voltage and choice of electrolyte may be prominent root causes of capacity fading of NCA at UCV >4.5V.
4. This study identifies the optimum upper-cut-off voltage as 4.5 V (vs. graphite and electrolyte without any additives for high-voltage operation) for NCA (performance of 92% capacity retention at 1C/-1C cycling rates over 100 full coin-cell cycles).

This study shows the potential of NCA to achieve ≥ 250mAh/g discharge capacity, but to improve the cycling stability of NCA above UCVs of 4.5 V, surface doping or coating to minimize the lattice contraction at high-voltage cycling and improvement in electrolyte stability must also be achieved.

Acknowledgement: This research at Oak Ridge National Laboratory, managed by UT Battelle, LLC, for the U.S. Department of Energy (DOE) under contract DE-AC05-00OR22725, was sponsored by the Office of Energy Efficiency and Renewable Energy (EERE) Vehicle Technologies Office (VTO) (Deputy Director: David Howell) Applied Battery Research subprogram (Program Manager: Peter Faguy). Part of this research (magnetic measurements) was supported by the DOE Basic Energy Sciences (BES), Materials Sciences and Engineering Division, and the SEM experiments were performed at ORNL's CNMS User Facility, which is sponsored by the DOE BES Scientific User Facilities Division.

Author contributions

D.M. pursued the idea, L.D and D.W. lead this research. L.D. and L.G. performed electrochemical and structural characterization and analyzed the data and wrote the manuscript. A.S. performed the magnetization experiment and involved in the discussion. E.K. did X-ray diffraction and was involved in diffraction analysis and discussion. H.M.M. performed the XPS experiments and was involved in XPS data analysis. H.W. performed DSC experiments. D.W. was also involved in the technical discussions and manuscript preparation.

References

[1] J. M. Tarascon, *Philos. Trans. R. Soc., A* **2010**, *368*, 3227-3241.

This article is protected by copyright. All rights reserved.

Accepted Manuscript

[2] V. Etacheri, R. Marom, R. Elazari, G. Salitra, D. Aurbach, *Energy Environ. Sci.* **2011**, *4*, 3243-3262.

[3] D. L. Wood, J. L. Li, C. Daniel, *J. Power Sources* **2015**, *275*, 234-242.

[4] A. Manthiram, Y. Fu, Y. S. Su, *J. Phys. Chem. Lett.* **2013**, *4*, 1295-1297.

[5] D. Mohanty, K. Dahlberg, D. M. King, L. A. David, A. S. Sefat, D. L. Wood, C. Daniel, S. Dhar, V. Mahajan, M. Lee, F. Albano, *Sci. Rep.* **2016**, *6*, 26532.

[6] A. Abdel-Ghany, K. Zaghib, F. Gendron, A. Mauger, C. M. Julien, *Electrochim. Acta* **2007**, *52*, 4092-4100.

[7] A. Mauger, F. Gendron, C. M. Julien, *J. Alloys Compd.* **2012**, *520*, 42-51.

[8] J. B. Goodenough, Y. Kim, *Chem. Mater.* **2009**, *22*, 587-603.

[9] D. Mohanty, B. Mazumder, A. Devaraj, A. S. Sefat, A. Huq, L. A. David, E. A. Payzant, J. Li, D. L. Wood, C. Daniel, *Nano Energy* **2017**, *36*, 76-84.

[10] C. Martin, *Nat. Nanotechnol.* **2014**, *9*, 327-328.

[11] S.-M. Bak, K.-W. Nam, W. Chang, X. Yu, E. Hu, S. Hwang, E. A. Stach, K.-B. Kim, K. Y. Chung, X.-Q. Yang, *Chem. Mater.* **2013**, *25*, 337-351.

[12] S.-T. M. Sun, M. Filippo, P. Kang-Joon, Y. Chong Seung, L. Peter, K. Sung-Jin, K. Yang, *ACS Energy Lett.* **2016**, *2*, 196-223.

[13] P. Keil, A. Jossen, *J. Electrochem. Soc.* **2017**, *164*, A6066-A6074.

[14] K.-J. Park, M.-J. Choi, F. Maglia, S.-J. Kim, K.-H. Kim, Ch. S. Yoon, Y.-K. Sun, *Adv. Energy Mater.* **2018**, *8*, 1703612.

[15] B. Delattre, R. Amin, J. Sander, J. De Coninck, A. P. Tomsia, Y.-M. Chiang, *J. Electrochem. Soc.* **2018**, *165*, A388-A395.

[16] S. Watanabe, M. Kinoshita, T. Hosokawa, K. Morigaki, K. Nakura, *J. Power Sources* **2014**, *260*, 50-56.

[17] L. Wu, K.-W. Nam, X. Wang, Y. Zhou, J.-C. Zheng, X.-Q. Yang, Y. Zhu, *Chem. Mater.* **2011**, *23*, 3953-3960.

[18] D. P. Abraham, R. D. Twesten, M. Balasubramanian, I. Petrov, J. McBreen, K. Amine, *Electrochem. Commun.* **2002**, *4*, 620-625.

[19] S. M. Bak, E. Hu, Y. Zhou, X. Yu, S. D. Senanayake, S. J. Cho, K. B. Kim, K. Y. Chung, X. Q. Yang, K. W. Nam, *ACS Appl. Mater. Interfaces* **2014**, *6*, 22594-22601.

[20] J. Li, R. Shunmugasundaram, R. Doig, J. R. Dahn, *Chem. Mater.* **2016**, *28*, 162-171.

Accepted Manuscript

This article is protected by copyright. All rights reserved.

[21] A. U. Liyanage, M. M. Lerner, *RSC Adv.* **2014**, *4*, 47121-47128.

[22] M. Guilmard, L. Croguennec, D. Denux, C. Delmas, *Chem. Mater.* **2003**, *15*, 4476-4483.

[23] F. Lin, D. Nordlund, Y. Li, M. K. Quan, L. Cheng, T.-C. Weng, Y. Liu, H. L. Xin, M. M. Doeff, *Nat. Energy* **2016**, *1*, 15004.

[24] F. Dogan, J. T. Vaughey, H. Iddir, B. Key, *ACS Appl. Mater. Interfaces* **2016**, *8*, 16708-16717.

[25] N. M. Trease, I. D. Seymour, M. D. Radin, H. Liu, H. Liu, S. Hy, N. Chernova, P. Parikh, A. Devaraj, K. M. Wiaderek, P. J. Chupas, K. W. Chapman, M. S. Whittingham, Y. S. Meng, A. Van der Van, C. P. Grey, *Chem. Mater.* **2016**, *28*, 8170-8180.

[26] D. Mohanty, S. Kalnaus, R. A. Meisner, K. J. Rhodes, J. Li, E. A. Payzant, D. L. Wood, C. Daniel, *J. Power Sources* **2013**, *229*, 239-248.

[27] D. Mohanty, S. Kalnaus, R. A. Meisner, A. S. Safat, J. Li, E. A. Payzant, K. Rhodes, I. I. I. D. L. Wood, C. Daniel, *RSC Adv.* **2013**, *3*, 7479-7485.

[28] N. A. Chernova, G. M. Nolis, F. O. Omenya, H. Zhou, Z. Li, M. S. Whittingham, *J. Mater. Chem.* **2011**, *21*, 9865-9875.

[29] J. T. Hertz, Q. Huang, T. McQueen, T. Klimczuk, J. W. G. Bos, L. Viciu, R. J. Cava, *Phys. Rev. B* **2008**, *77*, 075119.

[30] K. Numata, C. Sakaki, S. Yamanaka, *Solid State Ionics* **1999**, *117*, 257-263.

[31] C. M. Julien, A. Ait-Salah, A. Mauger, F. Gendron, *Ionics* **2006**, *12*, 21-32.

[32] W.-S. Yoon, K. Y. Chung, J. McBreen, X.-Q. Yang, *Electrochem. Commun.* **2006**, *8*, 1257-1262.

[33] D. Zeng, J. Cabana, W.-S. Yoon, C. P. Grey, *Chem. Mater.* **2010**, *22*, 1209-1219.

[34] A. M. Wise, C. Ban, J. N. Weker, S. Misra, A. S. Cavanagh, Z. Wu, Z. Li, M. S. Whittingham, K. Xu, S. M. George, M. F. Toney, *Chem. Mater.* **2015**, *27*, 6146-6154.

[35] Z. Chen, Z. Lu, J. R. Dahn, *J. Electrochem. Soc.* **2002**, *149*, A1604-A1609.

[36] H. Xia, L. Lu, Y. S. Meng, G. Ceder, *J. Electrochem. Soc.* **2007**, *154*, A337-A342.

Accepted Manuscript

This article is protected by copyright. All rights reserved.

10.1002/celc.201901338

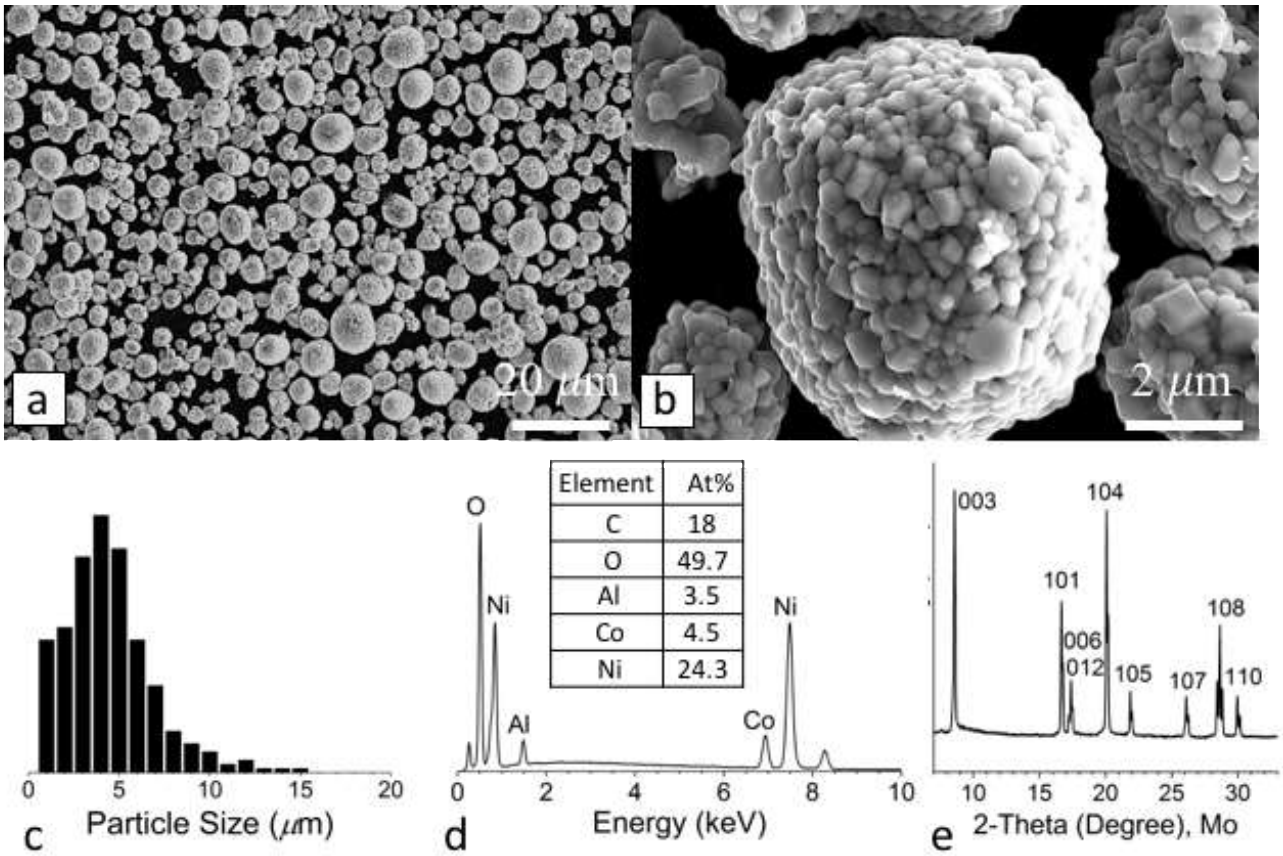

Figure 1. (a) Low resolution SEM image, (b) high resolution SEM image, (c) particle size distribution from the low-resolution SEM image, (d) EDS analysis from the high-resolution SEM image and (e) XRD of pristine NCA powder.

Accepted Manuscript

This article is protected by copyright. All rights reserved.

10.1002/celc.201901338

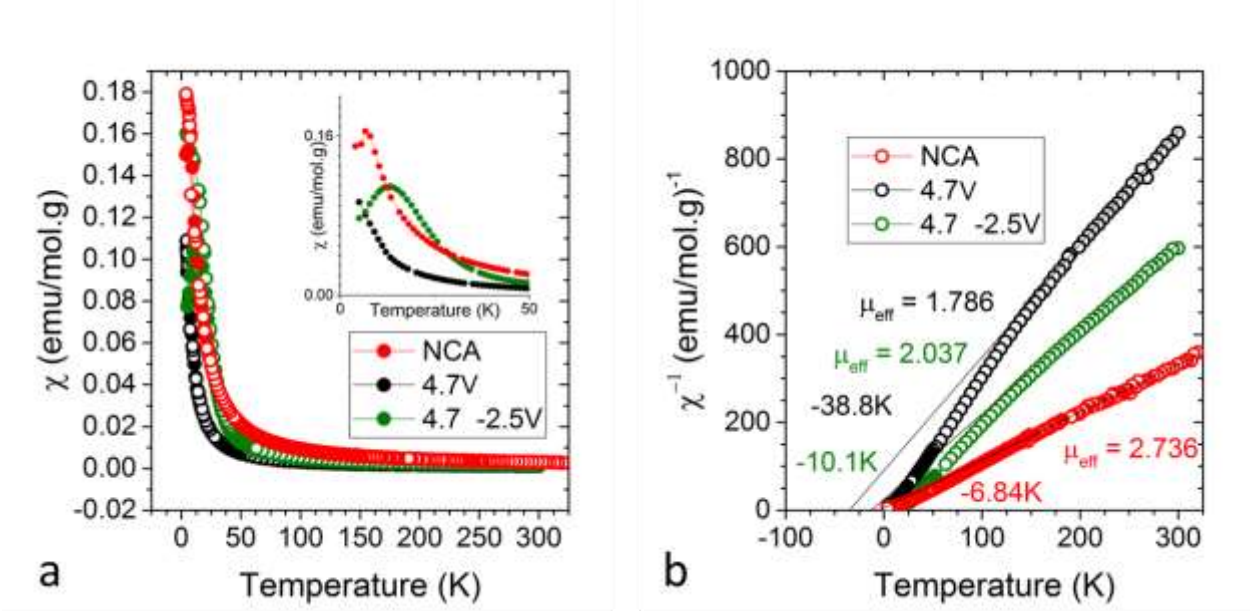

Figure 2. (a) Temperature dependent magnetic susceptibility data for pristine NCA electrode under zero field cooling (ZFC indicated with solid points) and field cooling (FC indicated with hollow points) modes compared with electrode harvested at the end of first charge cycle to 4.7 V and end of first cycle at 2.5 V. The insert shows the strong differences during ZFC mode between the pristine/discharged NCA and fully charged state at low temperature. (b) Corresponding Curie-Weiss fits to the inverse magnetic susceptibility data fitted at T = 100-320 K range showing the paramagnetic region.

Accepted Manuscript

This article is protected by copyright. All rights reserved.

10.1002/celc.201901338

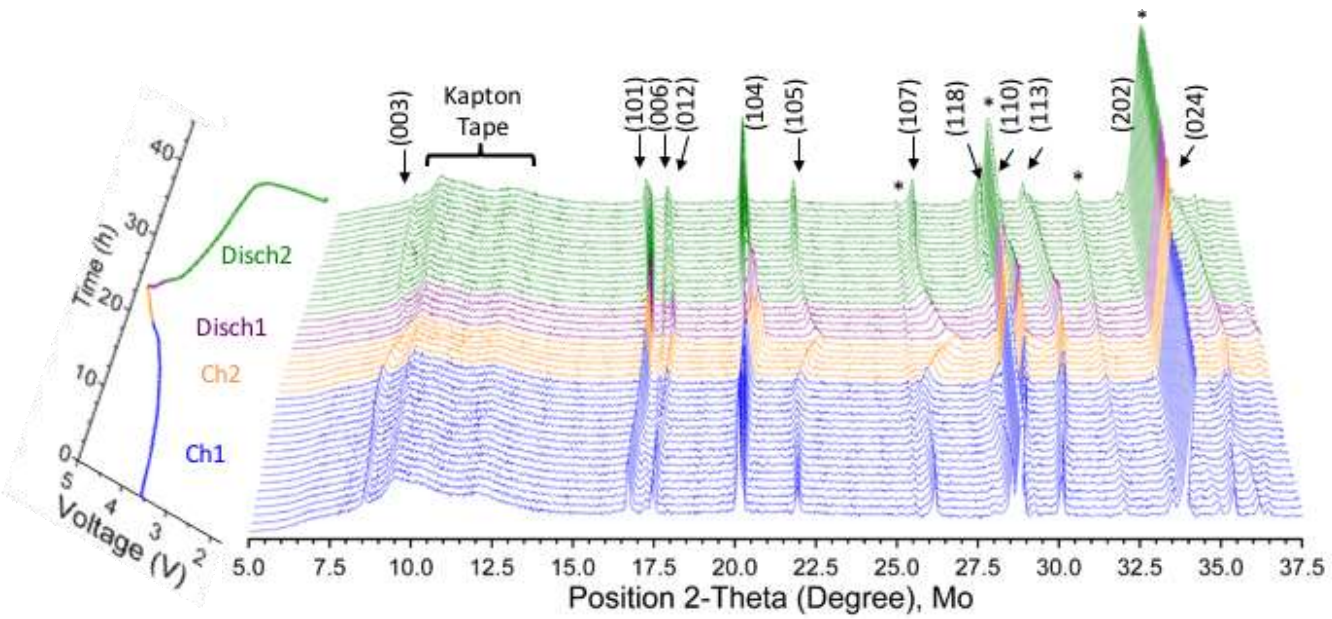

Figure 3. In-situ XRD plots during first cycle of NCA coin cell. All peaks are indexed to reflections associated with rhombohedral phase. The scans are color coded to different sections based on the charge/discharge characteristics of NCA.

Accepted Manuscript

This article is protected by copyright. All rights reserved.

10.1002/celc.201901338

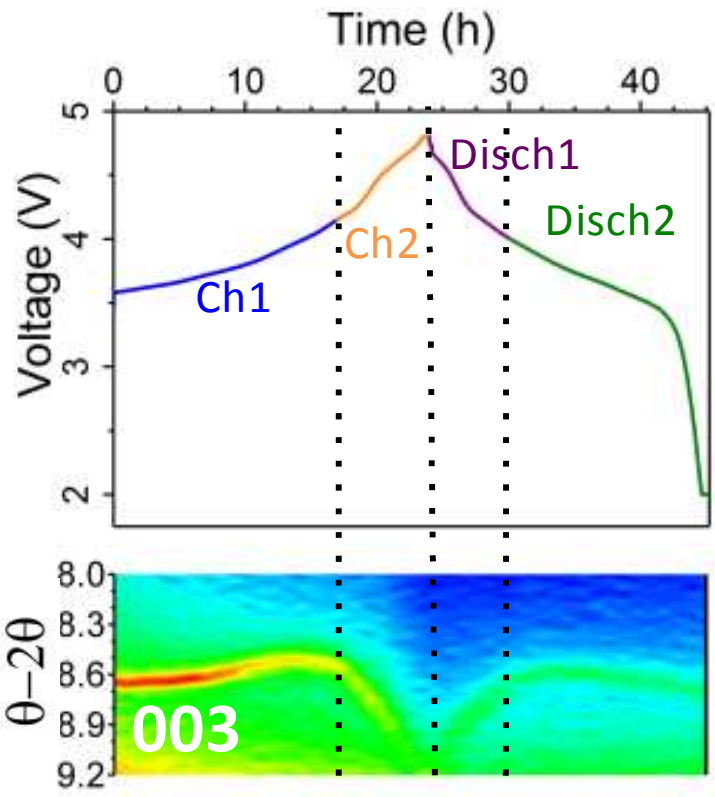

Figure 4. Intensity plots of (003) peak along with the electrochemical profile of the cell during the first cycles.

Accepted Manuscript

This article is protected by copyright. All rights reserved.

10.1002/celc.201901338

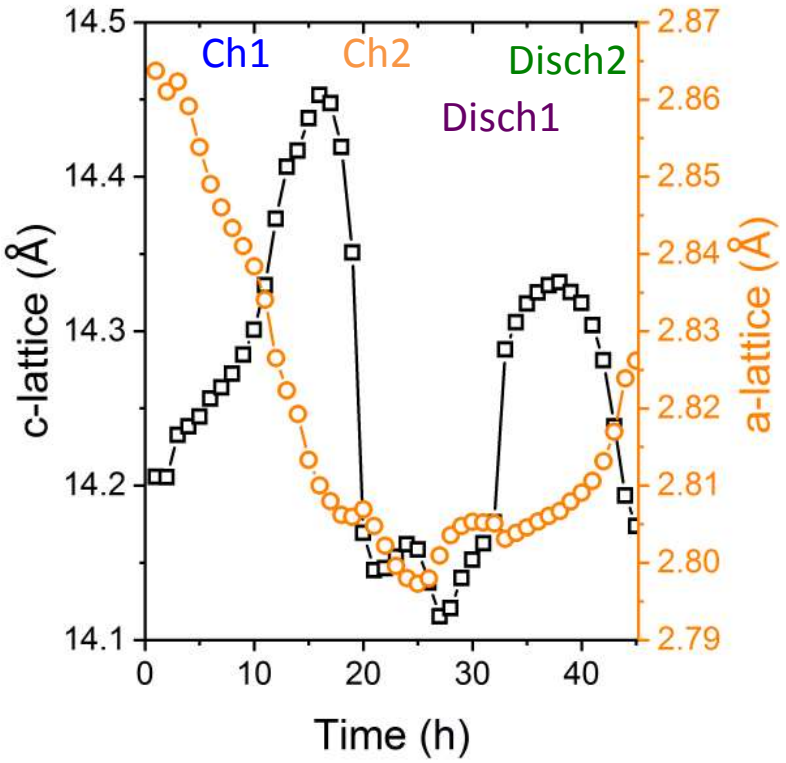

Figure 5. Calculated *a*- and *c*-lattice parameters from the *in-situ* XRD curves along with the electrochemical profile of the cell during the first two cycles.

Accepted Manuscript

This article is protected by copyright. All rights reserved.

10.1002/celc.201901338

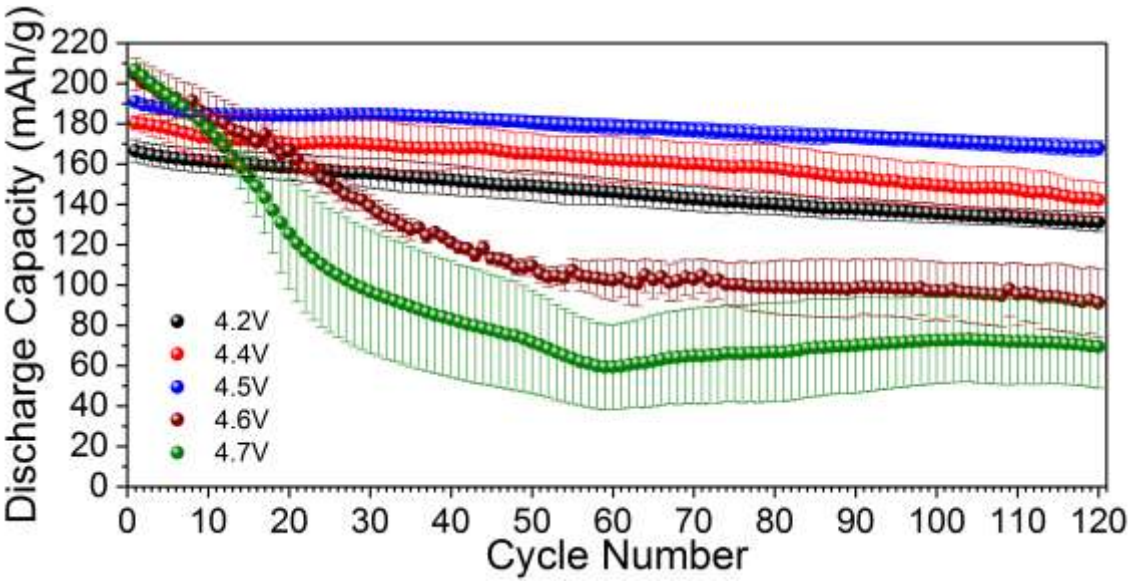

Figure 6. (a) Cycle life testing at 1C/-1C rate of cells that were cycled to various UCVs.

Accepted Manuscript

This article is protected by copyright. All rights reserved.

10.1002/celc.201901338

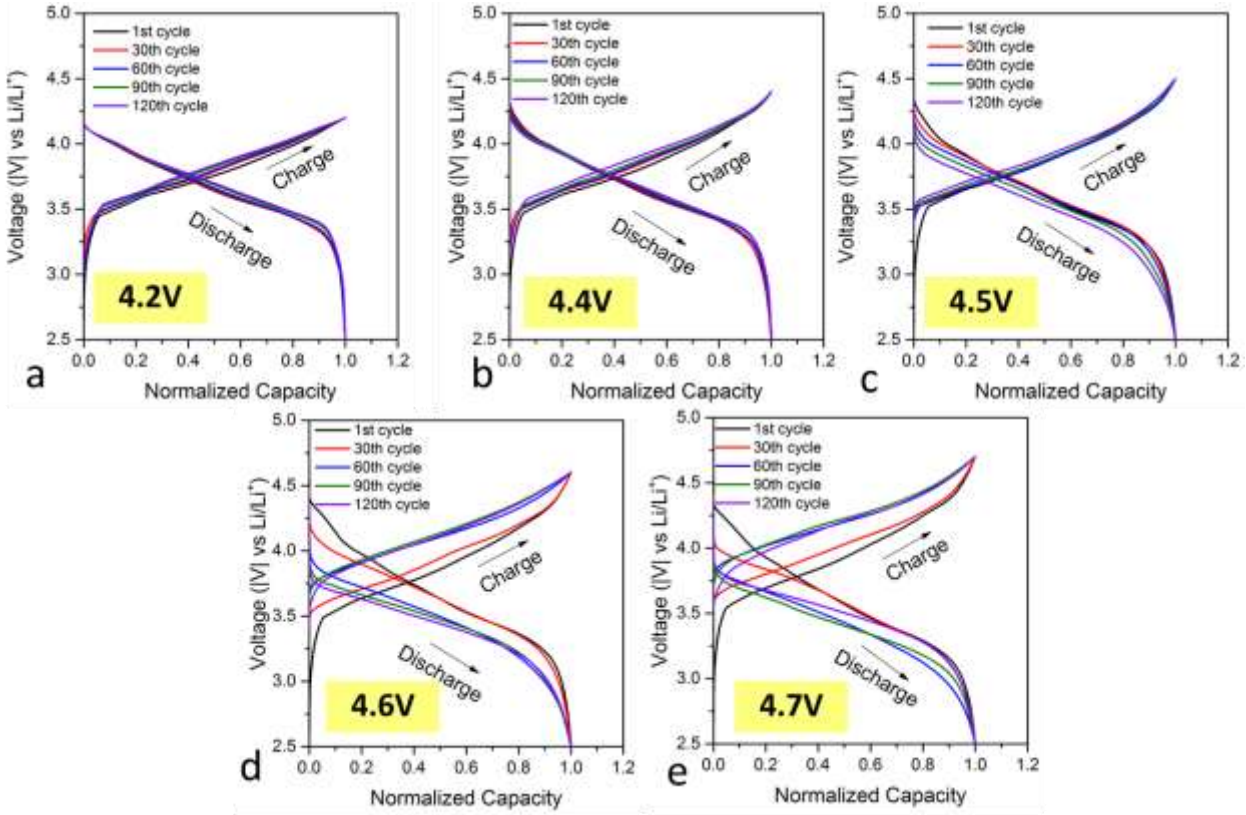

Figure 7. Normalized charge/discharge curves of NCA comparing 1st, 30th, 60th, 90th and 120th cycle to upper cut-off voltages of (a) 4.2 V, (b) 4.4 V, (c) 4.5 V, (d) 4.6 V and (e) 4.7 V.

Accepted Manuscript

This article is protected by copyright. All rights reserved.

10.1002/celc.201901338

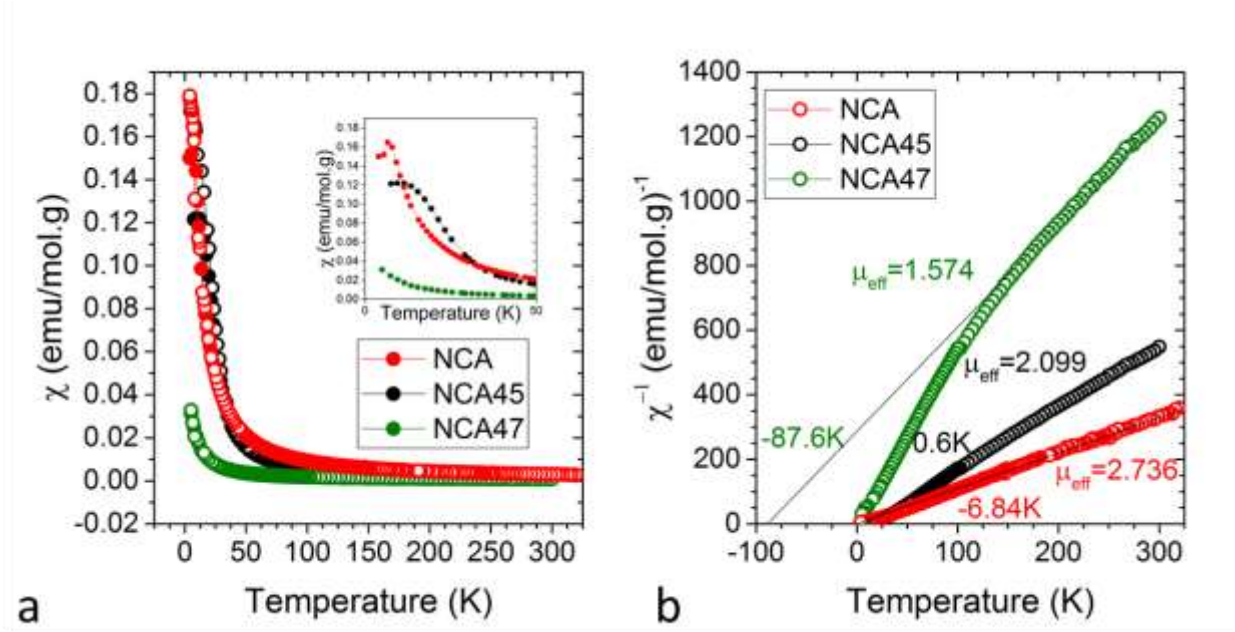

Figure 8. (a) Temperature dependent magnetic susceptibility data for pristine NCA electrode at zero field cooling (ZFC indicated with solid points) and field cooling (FC indicated with hollow points) modes compared with electrode harvested after 100 charge/discharge cycles to a UCV of 4.5 V and 4.7 Vat 1C/-1C rates. The insert shows the strong differences during ZFC mode between the different electrodes at low temperature. (b) Corresponding Curie-Weiss fits to the inverse magnetic susceptibility data fitted at T = 100-320 K range showing the paramagnetic region.

Accepted Manuscript

This article is protected by copyright. All rights reserved.

10.1002/celc.201901338

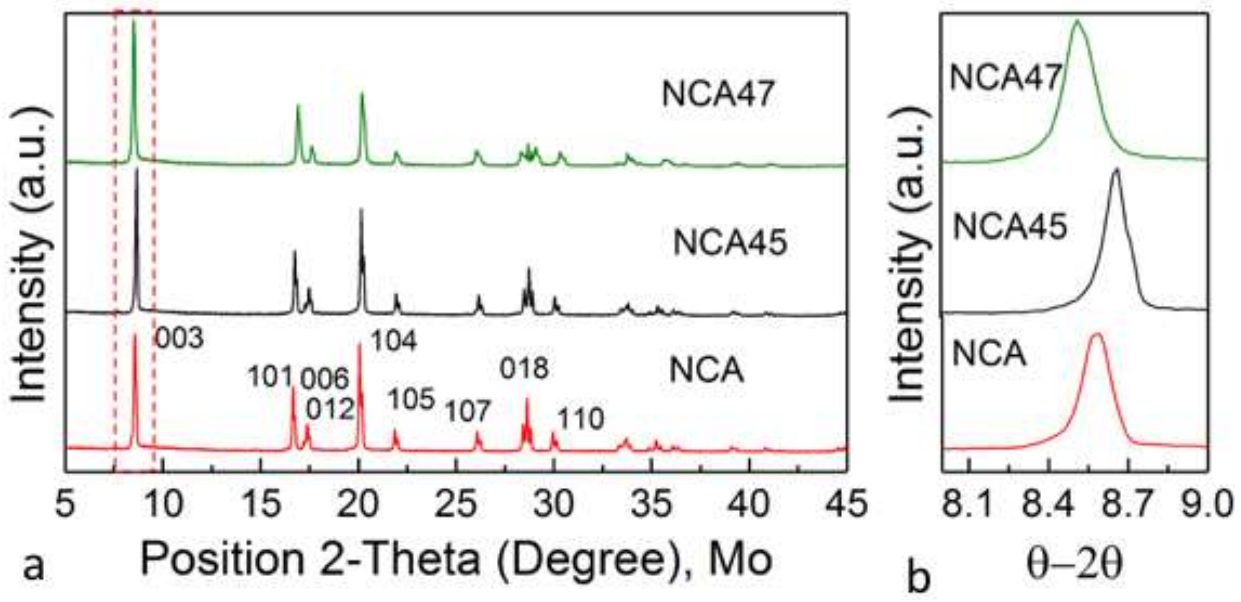

Figure 9. (a) Comparison of the *ex-situ* XRD of NCA electrodes cycled to 4.5 V and 4.7 V to the pristine NCA. (b) Magnified region of XRD comparing the 003 peak of the corresponding eelctrodes.

Accepted Manuscript

This article is protected by copyright. All rights reserved.

10.1002/celc.201901338

Table 1. Charge/discharge capacity and columbic efficiency at specific cycle numbers for cells cycled to different upper cut-off voltages during testing.

	Charge Capacity, mAh/g	Discharge Capacity, mAh/g	Efficiency, %
4.2 V			
1st Formation - C/20	215 ± 8	184 ± 8	85.5 ± 0.75
2nd Formation - C/20	187 ± 9	183 ± 8	97.9 ± 0.01
1st cycle - 1C	184 ± 9	167 ± 6	90.6 ± 1.24
2nd cycle - 1C	167 ± 6	166 ± 5	99.1 ± 0.10
120th cycle - 1C	132 ± 5	132 ± 5	99.6 ± 0.01
4.4 V			
1st Formation - C/20	243 ± 4	204 ± 5	87.1 ± 0.88
2nd Formation - C/20	207 ± 5	204 ± 6	98.3 ± 0.27
1st cycle - 1C	204 ± 6	180 ± 3	88.4 ± 0.87
2nd cycle - 1C	182 ± 3	180 ± 5	99.1 ± 0.76
120th cycle - 1C	144 ± 9	143 ± 9	99.8 ± 0.11
4.5 V			
1st Formation - C/20	240 ± 2	205 ± 1	85.3 ± 0.67
2nd Formation - C/20	212 ± 1	208 ± 1	97.8 ± 0.05
1st cycle - 1C	214 ± 3	191 ± 1	89.3 ± 1.17
2nd cycle - 1C	194 ± 2	189 ± 1	97.8 ± 1.43
120th cycle - 1C	168 ± 4	168 ± 4	99.7 ± 0.02
4.6 V			
1st Formation - C/20	264 ± 10	224 ± 6	84.9 ± 0.96
2nd Formation - C/20	231 ± 5	224 ± 5	97.2 ± 0.07
1st cycle - 1C	226 ± 4	212 ± 6	93.7 ± 0.84
2nd cycle - 1C	212 ± 6	210 ± 6	98.7 ± 0.11
120th cycle - 1C	110 ± 2	108 ± 1	98.8 ± 0.81
4.7 V			
1st Formation - C/20	259 ± 1	223 ± 1	86.1 ± 0.73
2nd Formation - C/20	229 ± 1	224 ± 2	97.6 ± 0.46
1st cycle - 1C	225 ± 2	204 ± 3	90.7 ± 0.56
2nd cycle - 1C	204 ± 3	201 ± 4	98.5 ±0.45
120th cycle - 1C	90 ± 13	89 ± 13	98.7 ± 0.66

Accepted Manuscript

This article is protected by copyright. All rights reserved.

10.1002/celc.201901338

Graphical Abstract:

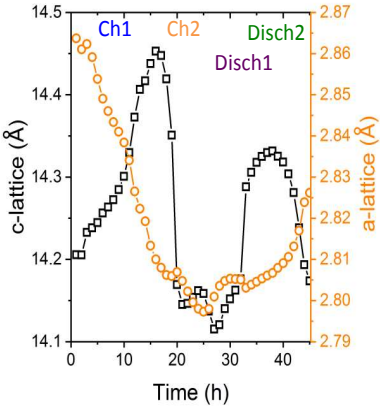

NCA lattice contraction occurs during high voltage cycling, which may indicate the gliding of lattice planes due to atomic structural rearrangement/modification. This phenomenon may not completely destroy the material lattice structure in the first cycle. However, the extent of lattice contraction (at higher UCV) may initiate permanent altering of the host NCA structure and cause an increase in capacity fading rate.

Key words: Li-ion battery, Ni-rich cathodes, *in-situ* XRD, lattice contraction, capacity fade.

Accepted Manuscript

This article is protected by copyright. All rights reserved.